The benefit of the facile charge-transfer capabilities of the conductive $BaFeO_4$ salt is evident in a cylindrical cell configuration (Fig. 4). Discharged to 1 V at 0.7 W high constant power, the $BaFeO_4$ cell provides 200% higher energy compared to advanced MnO_2 alkaline cylindrical AAA cells (0.86 W·hours compared to 0.285 W·hours). Common cylindrical cells range in volume from approximately 3 to 50 cm^3 for AAA up to D-type configurations. This geometry requires an increase in material scale by two orders of magnitude compared to the simple "button" configuration, and provides an ongoing challenge in cell optimization. Industry regularly reports incremental increases in alkaline cylindrical MnO_2/Zn energy density and, most recently, has reported advances in the high-power discharge domain. One recent posted advanced result is determined at constant power discharge (Fig. 4, inset) (*17*). Compared to these conventional advanced alkaline cells, the $BaFeO_4$ cell provides a 200% higher energy capacity under high-drain (0.7 W discharge) and a 40% increased capacity under low-drain (0.08 W) conditions. The cylindrical $BaFeO_4$ cell uses the conventional cell Zn anode mix, anode current collector, and separator. In future experiments, with specific optimization for the super-iron cell, further energy capacity increases are expected.

Conventional MH batteries, with a capacity up to 95 W·hours/kg (*5*), compared to 40 W·hours/kg for NiCd, have advanced to where further energy storage improvements are largely limited by the cell's heavy nickel oxyhydroxide (NiOOH) cathode. This situation is analogous to the limitations of MnO_2 for primary Zn batteries and is accentuated by the lower limiting NiOOH cathode capacity of ~290 mA·hours/g. These important secondary (rechargeable) batteries use alkaline KOH electrolyte.

We have also probed the reversible nature of Fe(VI) chemistry. An Fe(VI) charge-limited open-cell experiment provides fundamental evidence that the Fe(VI) cathode is significantly rechargeable. The cell has been discharged to 75% cathode capacity depth of discharge (DOD) for several cycles and more than 400 cycles at 30% DOD. The cell consists of an excess of MH anode (35 mA·hours, removed from a GP 35BVH button cell), and a limiting Fe(VI) cathode (9 mA·hours based on 406 mA·hours/g K_2FeO_4, using a Teflon mesh pressed over the K_2FeO_4 mix), in excess 12 M KOH electrolyte. The cell potential varies from 1.3 V (open circuit) to 1.1 V (at 5 mA/cm^2) and is cycled at 2.5 mA charge and 1 mA discharge. This cell has a characteristic voltage similar to the conventional MH battery because of the similarity of the Fe(VI) potential to the 0.5 V formal potential of NiOOH.

In the primary-battery studies, the AAA cell configuration has been used only to provide a clear comparison to existing optimized electrochemistries. The engineering of MnO_2 into a conventional cylindrical cell is an ongoing process which has taken many decades. Engineering studies of the new Fe(VI) cathode will also be an ongoing process. Further research probing, stabilizing, and releasing the substantial storage of other Fe(VI) cathodes will be needed. For example, a composite high-capacity Fe(VI) cathode containing several Fe(VI) salts also exhibits efficient discharge in the high-current domain, and, as in the K_2FeO_4 and $BaFeO_4$ cells in this study, generates significantly greater energy capacity than in conventional alkaline batteries.

References and Notes

1. J. R. Dahn, T. Zheng, Y. Liu, J. S. Xue, *Science* **270**, 590 (1995).
2. Y. Idota, T. Kubota, A. Matsufuji, Y. Maekawa, T. Miyasaka, *ibid.* **276**, 1395 (1997).
3. E. Reddington *et al.*, *ibid.* **280**, 1735 (1998).
4. B. T. Holland, C. F. Blanford, A. Stein, *ibid.* **281**, 538 (1998).
5. S. R. Ovshinsky, M. A. Fetcenko, J. Ross, *ibid.* **260**, 176 (1993); S. K. Dhar *et al.*, *J. Power Sources* **65**, 1 (1997).
6. Z. Rong *et al.*, *Science* **276**, 926 (1997).
7. D. Peramunage and S. Licht, *ibid.* **261**, 1029 (1993).
8. S. Licht, D. Peramunage, N. Myung, *J. Phys. Chem. B.* **102**, 6780 (1998).
9. M. D. Johnson and J. F. Read, *Inorg. Chem.* **35**, 6795 (1996).
10. J. D. Carr *et al.*, Proceedings of the 5th Conference, *Water Chlorination*, Williamsburg, VA, 3 to 8 June 1984, R. L. Jolley, Ed., (Lewis, Chelsea, MI, 1985), pp. 1285–1298; V. K. Sharma, J. O. Smith, F. J. Millero, *Environ. Sci. Technol.* **31**, 2486 (1997).
11. M. D. Johnson and B. Hornstein, *Chem. Commun.* **1996**, 965 (1996).
12. L. Delaude and P. A Laszlo, *J. Org. Chem.* **61**, 6360 (1996).
13. Using analytical grade reagents of 97 to 99% purity, K_2FeO_4 was synthesized from alkaline hypochlorite treatment of $Fe(NO_3)_3$ as described in (*12*). The dried product is stable in time. The $BaFeO_4$ was synthesized from 0.25 M (97 to 99% pure) K_2FeO_4 dissolved in 2% KOH solution at 0°C, and filtered into an equivalent volume of 0.39 M (analytical grade) $Ba(C_2H_3O_2)_2$ solution at 0°C. Solutions were prepared without CO_2 in deionized water. The precipitate was filtered, washed with water, and freeze dried (using a Labconco Lyph-Lock Freeze Dry System), producing 98.5 ± 0.5% purity $BaFeO_4$. The Li_2FeO_4, Na_2FeO_4, and Cs_2FeO_4 were prepared in a manner similar to K_2FeO_4 (hypochlorite oxidation) but yielded lower purity. The $SrFeO_4$, Ag_2FeO_4 $MgFeO_4$, $CaFeO_4$, and $ZnFeO_4$ were investigated in a manner similar to $BaFeO_4$ (precipitation from a K_2FeO_4 solution) but yielded lower purity.
14. J. Chen and H. Y. Che, *J. Electrochem. Soc.* **140**, 1205 (1993).
15. J. Veprek-Siska and V. Ettel, *Chem. Ind.* **1967**, 548 (1967).
16. S. Licht, B. Wang, S. Ghosh, data not shown.
17. Duracell Web site, file MX2400.pdf (ULTRA vs. Standard AAA) downloaded 24 June 1999. (www.duracell.com/OEM/Primary/Alkaline/alkaline_manganese_data.html.)

18. We thank V. Naschitz, J. Li, S. Shesternin, and V. Nair, who participated in synthesis of the Fe(VI) compounds, and G. Xu, V. Goldstein, O. Khaselev, and E. Kvashnina who participated in cell discharges.

25 May 1999; accepted 2 July 1999

Phonon- Versus Electron-Mediated Desorption and Oxidation of CO on Ru(0001)

M. Bonn,* S. Funk, Ch. Hess, D. N. Denzler, C. Stampfl, M. Scheffler, M. Wolf, G. Ertl

Heating of a ruthenium surface on which carbon monoxide and atomic oxygen are coadsorbed leads exclusively to desorption of carbon monoxide. In contrast, excitation with femtosecond infrared laser pulses enables also the formation of carbon dioxide. The desorption is caused by coupling of the adsorbate to the phonon bath of the ruthenium substrate, whereas the oxidation reaction is initiated by hot substrate electrons, as evidenced by the observed subpicosecond reaction dynamics and density functional calculations. The presence of this laser-induced reaction pathway allows elucidation of the microscopic mechanism and the dynamics of the carbon monoxide oxidation reaction.

The catalytic oxidation of CO on transition metal surfaces is technologically very important, being a key reaction, for example, in automotive exhaust catalysts. To fully understand this surface reaction—ideally leading to better and more efficient catalytic processes—requires insight on atomic length (angstrom) and reaction time (femtosecond) scales. Structural information with the required spatial resolution has recently been obtained by means of scanning probe techniques (*1*), but the ultrafast dynamics (*2*) of such reactions are still largely unexplored,

Fritz-Haber-Institut der Max-Planck-Gesellschaft, Faradayweg 4-6, 14195 Berlin, Germany.

*To whom correspondence should be addressed. E-mail: bonn@fhi-berlin.mpg.de

despite recent progress with femtosecond spectroscopic investigations, such as on the Pt(111) surface (*3*, *4*).

Here we elucidate the mechanism and the subpicosecond dynamics of the oxidation of CO on Ru(0001), a well-documented model system (*5*). The reaction is initiated by excitation of the surface on which CO and atomic O are coadsorbed, with near-infrared (800 nm = 1.5 eV) laser pulses of 110-fs duration. It is important to note that CO_2 cannot be formed thermally (that is by heating the surface) under ultrahigh vacuum conditions. This means that a new reaction path is opened by the femtosecond laser excitation.

In the traditional picture of a thermal reaction on a metal surface, the phonons drive the system across the activation barrier in the electronic ground state. However, electrons in the high-energy tail of a thermal Fermi-Dirac distribution can also induce chemical transformations by transient population of normally unoccupied states, as demonstrated here. Such phonon- and electron-mediated processes are fundamentally different, but cannot be distinguished with conventional heating, where electrons and phonons are in equilibrium. With femtosecond laser excitation, we exploit the strong nonequilibrium between electrons and phonons to separate electron- from phonon-induced processes, allowing us to establish reaction mechanisms and key reaction parameters such as the pathways and subpicosecond time scales of energy flow.

The Ru(0001) surface was first covered with 0.5 monolayers of atomic O [(2 × 1)-O/Ru(0001)] by exposure to 5-Langmuir (1 Langmuir = 10^{-6} torr·s) O_2, after which 1.8-Langmuir CO was dosed [preparation and characterization are described in (*6*)]. In the following, this surface will be referred to as CO/O/Ru(0001). The O coverage depletion is below 10^{-3} per laser shot. Formation of CO_2 from reaction of surface O with gas phase CO (Eley-Rideal mechanism) does not take place: The two reactants have to be coadsorbed on the surface for oxidation to occur (Langmuir-Hinshelwood mechanism). Time-of-flight spectra (Fig. 1A) show the formation of CO_2 and CO after femtosecond-laser excitation. The branching ratio between desorption and oxidation (yield[CO]/yield[CO_2]) is 35 ± 2.5 (σ).

Excitation of a Ru surface with a femtosecond infrared laser pulse can lead to substrate-mediated chemical changes at the surface according to the following mechanism (Fig. 1B). The laser pulse excites the electrons near the metal surface (optical penetration depth ~10 nm), and rapid thermalization within the electron gas to a hot Fermi-Dirac distribution occurs by electron-electron scattering. Because of the very small electronic heat capacity, peak electronic temperatures of thousands of Kelvin above the equilibrium melting point can be reached (Fig. 1B).

Subsequent cooling of electrons occurs simultaneously by diffusive electron transport into the bulk and by electron-phonon coupling, characterized by a coupling time $\tau_{el\text{-}ph}$ (≈300 fs for Ru). A surface reaction can then be triggered either by coupling of the adsorbate to these hot electrons (coupling time τ_{el}), or by coupling to phonons (coupling time τ_{ph}). Energy exchange with electrons involves the transfer of electrons from the substrate to the adsorbate (transient population of normally unoccupied adsorbate orbitals), by which energy is transferred to the adsorbate. In contrast, reactions caused by phonons take place in the electronic ground state, and energy is transferred from the phonons to adsorbate vibrations that are coupled to the reaction coordinate. The nonequilibrium between electrons and phonons upon excitation with an ultrashort laser pulse allows for the distinction between electron- and phonon-induced processes, which is not possible with conventional heating. The predominant coupling path can be determined by means of a two-pulse correlation measurement (*7*). In such experiments, the photo-reaction yield is measured as a function of the delay between two pulses of equal intensity. Because of the fast electron-phonon coupling, high electronic temperatures resulting from the combined effect of the two pulses can only be reached when the two pulses are separated by a time-span that

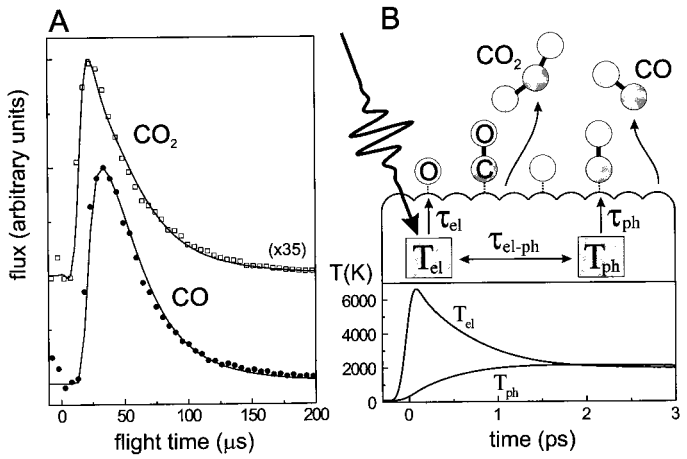

Fig. 1. (**A**) CO and CO_2 time-of-flight spectra (CO_2 signal multiplied by 35), demonstrating the formation of CO_2 and desorption of CO after pulsed excitation of CO/O/Ru(0001). Translational temperatures obtained from the fitted lines are 640 and 1590 K for CO and CO_2, respectively. (**B**) Process of laser-induced surface chemistry. The laser pulse heats the electrons, leading to a very high transient electronic temperature, T_{el}. Electron-phonon coupling leads to equilibration of the energy in ~1 ps. The surface reaction can occur by coupling to either the hot electrons or to the phonons. T_{el} and T_{ph} are calculated as described in (*15*).

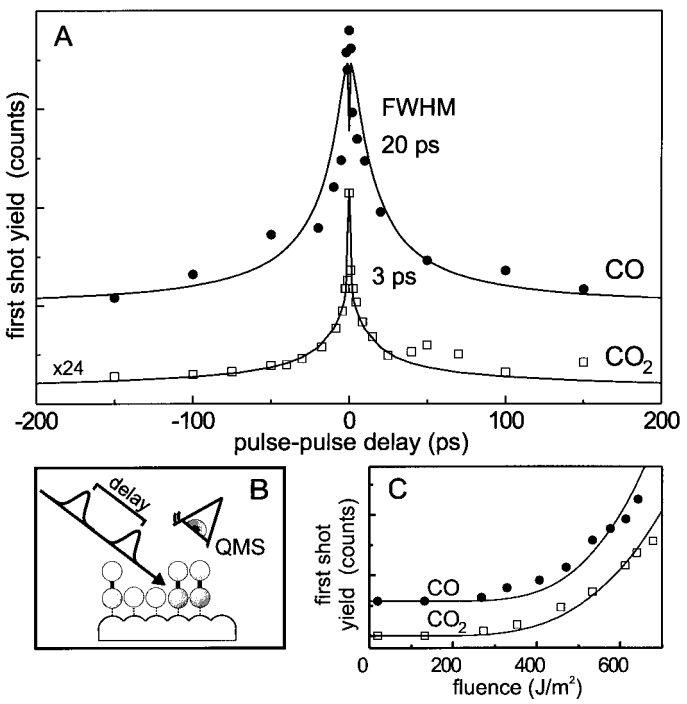

Fig. 2. (**A**) Two-pulse correlation measurements for the laser-induced oxidation (yielding CO_2, □; signal multiplied by 24) and desorption of CO (●) from CO/O/Ru(0001). Full widths at half maximum (FWHM) refer to experimental data. The response for CO_2 formation is an order of magnitude faster than for CO desorption. (**B**) Principle of the two-pulse correlation technique. The yield is measured as a function of delay between two excitation pulses. (**C**) The nonlinear fluence dependence of the yields for the two competing processes demonstrate that the branching ratio between desorption and oxidation is independent of the absorbed fluence within experimental error. Lines in the two-pulse correlation and fluence dependence data are the result of friction model calculation with the same parameter sets.

does not exceed the electron-phonon equilibration time of ~1 ps. Therefore, one expects a fast response of a few picoseconds in the two-pulse correlation experiment if the reaction is electron-mediated. In contrast, a slow response indicates predominant coupling to phonons, because the cooling of phonons is much slower (~50 ps). The results of such experiments for the desorption and oxidation of CO from CO/O/Ru(0001) (Fig. 2A) show that the time scales for the two competing processes differ by almost an order of magnitude. The ultrafast response for the oxidation of 3-ps full width at half maximum (FWHM) suggests that this reaction is driven by the hot electrons, whereas the much slower response for desorption of 20 ps implies coupling to phonons.

That the oxidation reaction is electron-mediated is verified by a pronounced isotope effect for this reaction. When the Ru surface is first covered with a 50/50 mixture of ^{16}O and ^{18}O, CO_2 containing the light O isotope is preferentially formed (yield ratio $^{16}OCO/^{18}OCO$ = 2.2 ± 0.3). This isotope effect can be rationalized in terms of multiple electronic transitions (*8*): The energetic metal electrons can be scattered into an unoccupied orbital of the O atom. The resulting short-lived, negatively charged O will favor a Ru–O distance different from that of the neutral state, so that the O atom is accelerated with respect to the surface. The electron residence time is equal for both isotopes, and thus the lighter isotope will traverse a larger distance than the heavier isotope, because it is accelerated faster. This means that when the electron transfers back to the substrate, leaving the O in its electronic ground state, the light isotope is further from its equilibrium position and has therefore acquired more vibrational energy that is available for surmounting the reaction barrier. Hence the larger yield for the lighter isotope. Several of these electronic excitation/de-excitation cycles can occur, increasing the reaction probability. An isotope effect of similar magnitude has been observed for electron-stimulated desorption of O^- ions from tungsten (*9*), explained by single electronic transitions. For phonon-mediated processes isotope effects are expected to be very small (*10*), consistent with the absence of an isotope effect for the phonon-mediated desorption reaction ($^{12}C^{16}O$ and $^{13}C^{18}O$, yield ratio of 0.98 ± 0.1) (*11*). Also, no isotope effect was observed for the oxidation reaction with respect to the CO mass.

Besides confirming that the oxidation reaction is electron-mediated, the O-isotope effect demonstrates that activation of the Ru–O bond by electrons is the rate-determining step in the oxidation reaction: As soon as the adsorbed O atoms are vibrationally activated by the hot substrate electrons (the amount of energy uptake being mass-dependent), the reaction can take place. Because of the high coverage, O and CO are in close proximity on the surface (3.52 Å) (*6*), and the required additional decrease in O–CO distance is easily realized by the thermally activated lateral motion of CO.

To obtain insight into the microscopic mechanism of the electron-induced activation, we carried out electron temperature–dependent density functional calculations (*12*) for O on Ru. We investigated the (2×1)-O/Ru(0001)

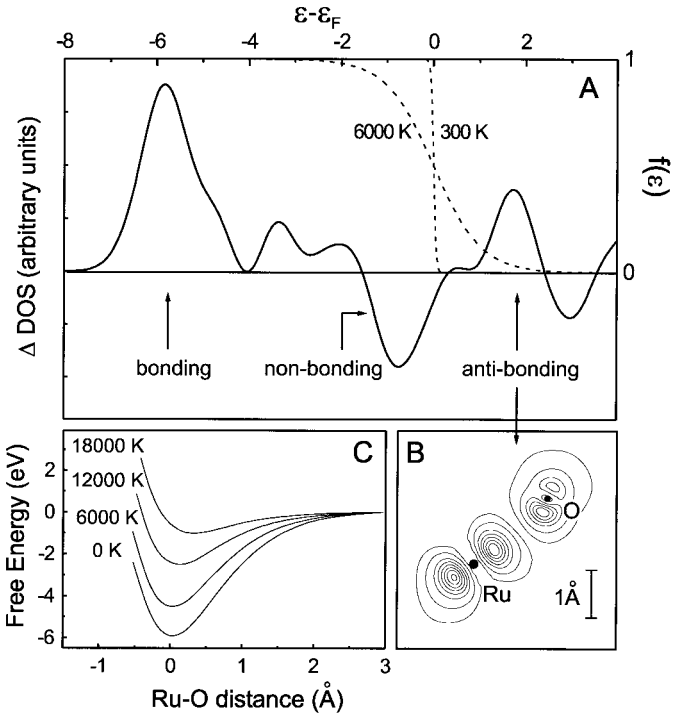

Fig. 3. Results of density functional theory calculations (*12*) for atomic O(2×1) on Ru. (**A**) The change in the density of states (DOS) upon adsorption of 0.5 ML of atomic O upon Ru(0001). A bonding state appears well below the Fermi level, ε_F, and an antibonding state 1.7 eV above ε_F. Fermi functions $f(\varepsilon)$ (right ordinate axis) at 300 and 6000 K demonstrate that with increasing temperature this level becomes populated. (**B**) Electron density (ψ^2) illustrating the antibonding character of the 1.7-eV state. (**C**) Free energy as a function of Ru–O distance and electronic temperature. The bond is strongly weakened as the electron temperature increases. These curves are obtained by evaluating the free energy as a function of distance of the O adlayer from the surface for different values of the electronic temperature, where the surface Ru atoms are held fixed at their bulk terminated positions.

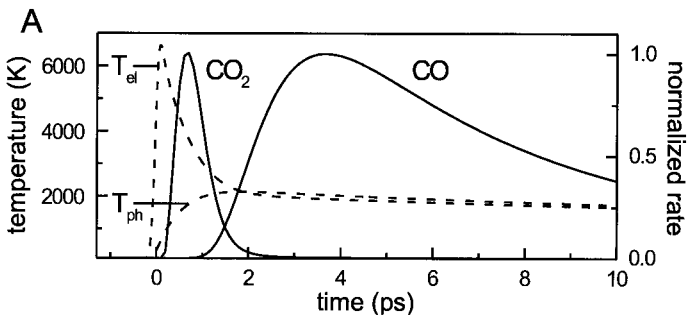

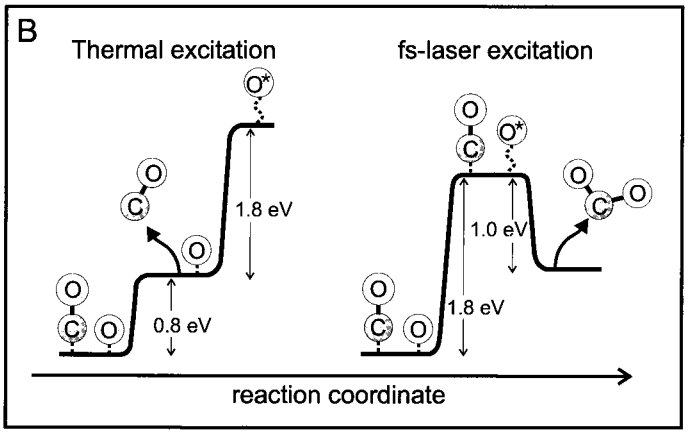

Fig. 4. (**A**) Calculated reaction rates (normalized, solid lines) for the oxidation of CO driven by the hot electrons and for the phonon-mediated desorption of CO, along with the time evolution of the electron and phonon temperatures (dashed lines) after excitation with a femtosecond pulse at t = 0. The formation of CO_2 is faster and almost complete before the desorption of CO is initiated. (**B**) Sketch illustrating that only desorption occurs when the system is excited thermally, as a result of the lower energy required for CO desorption than for O activation. Under laser excitation, the 1.8-eV barrier for O activation is overcome by coupling to the hot electrons, so that CO_2 can be formed.

system using a (2×2) surface unit cell with four atomic layers of Ru and the O atoms on one side of the slab. Upon adsorption of O, an unoccupied state right above the Fermi level ε_F is induced (Fig. 3A). This state is antibonding with respect to the Ru–O bond, as demonstrated by the node in the electron wave function between the Ru and the O atoms (Fig. 3B). Hot metal electrons can populate this antibonding orbital (whereas below ε_F only nonbonding orbitals are depopulated), which means that heating of the electrons leads to a weakening of the Ru–O bond (Fig. 3C): With increasing T_{el}, the minimum in the free energy increases and simultaneously the Ru–O equilibrium distance increases. This softening of the Ru–O bond with increasing electronic temperature is precisely the electron-induced activation observed in our experiment leading to CO oxidation.

To extract activation energies and coupling rates, we have modeled our data using the friction model (*13*, *14*). This model describes the system as coupled heat baths of electrons, phonons, and the adsorbate, characterized by (time-dependent) temperatures T_{el}, T_{ph}, and T_{ads}, respectively. T_{el} and T_{ph} are calculated by means of a two-temperature model (*15*), which includes diffusive heat transport and electron-phonon coupling. T_{ads} changes as a result of coupling to the electron and phonon heat baths, where the rate of heat transfer is determined by τ_{el} (*16*) and τ_{ph}, respectively (Fig. 1B). The theory predicts an isotope dependence for τ_{el} [proportional to the adsorbate mass (*13*)] through the mechanism described above. The increased adsorbate temperature then gives rise to a reaction at the surface, which is modeled by an Arrhenius-type expression for the reaction rate: $R(t) \propto \exp[-E_a/k_B T_{ads}(t)]$, where E_a is the activation energy and t is the time. The yield measured in the experiment is the time-integrated reaction rate $R(t)$.

For the oxidation, a consistent description of both the two-pulse correlation trace and the fluence dependence is achieved by adjusting the activation energy to $E_a = 1.80 \pm 0.15$ eV and the coupling time to $\tau_{el} = 0.5 \pm 0.1$ ps. The lines in Fig. 2, A and C, show the resulting excellent agreement between theory and experiment. With these parameters, the theory predicts an isotope effect of 1.6, in reasonable agreement with the experimentally observed value of 2.2 ± 0.3. The activation energy of the Ru–O bond of $E_a = 1.8$ eV is appreciably lower than the 4.9-eV Ru–O bond strength (*17*), which has to be weakened for reaction.

For the desorption, we use the value $E_a = 0.83$ eV obtained from thermal desorption measurements (*6*, *18*), because the process is phonon-mediated and therefore "thermal." Both the two-pulse correlation trace and the fluence dependence can be reproduced very well with this value, a coupling time to phonons of $\tau_{ph} = 1.0^{+3.0}_{-0.5}$ ps, and no coupling to the electrons (Fig. 2, A and C). The relative insensitivity to the exact value of τ_{ph} is due to the slow temperature dynamics of the phonons.

The different activation mechanisms for the two competing reactions (the desorption is phonon-driven, whereas the oxidation is electron-mediated) further imply that the temporal evolution of the two reactions is different. This is illustrated in Fig. 4A, which depicts the rate of CO_2 formation and of CO desorption after excitation with a laser pulse, calculated with the model described above. The oxidation reaction requires an electron-mediated excitation of the Ru–O bond that is most efficient during the short time in which the electrons are at their peak temperature. The phonon-mediated mechanism active in the desorption is much slower, because the phonon temperature peaks later than the electronic temperature and decays much more slowly. Clearly, the oxidation is almost complete when the desorption begins. It is this separation of time scales that enables the oxidation to take place upon femtosecond excitation.

The thermal and laser-induced processes are schematically illustrated in Fig. 4B. For oxidation to occur, the Ru–O bond needs to be activated, after which the reaction with coadsorbed CO takes place. However, the energy required for CO desorption [$E_a = 0.83$ eV (*6*)] is considerably lower than the barrier for CO_2 formation ($E_a = 1.8$ eV), so that attempts to drive the reaction thermally fail because CO is desorbed before the O is activated to react. In contrast, laser excitation enables the oxidation reaction through excitation of the Ru–O bond by the laser-heated Ru electrons, allowing the system to overcome the 1.8-eV barrier leading to CO_2, before the phonons are sufficiently hot to cause CO to desorb. Thus, the competing process of desorption is outpaced: Upon laser excitation, we can bring the system into regions of the potential energy surface that are thermally not accessible, resulting in a novel reaction pathway.

This work demonstrates that electrons can chemically activate adsorbates, suggesting that for thermally driven reactions this mechanism might also be operative, in contrast to the traditional view where activation occurs solely by phonons. Although the extremely hot electron distribution is unique to femtosecond excitation, it persists for only ~1 ps, whereas the interaction time with conventionally heated (but cooler) electrons is orders of magnitude longer. As a consequence, in a thermal reaction, activation by electrons in the high-energy tail of the distribution cannot be excluded; it will depend on the exact electronic structure of the adsorbate.

References and Notes

1. W. Ho, *Acc. Chem. Res*. **31**, 567 (1998); J. Wintterlin, S. Völkening, T. V. W. Janssens, T. Zambelli, G. Ertl, *Science* **278**, 1931 (1997); J. K. Gimzewski and C. Joachim, *ibid.* **283**, 1683 (1999).
2. H.-L. Dai and W. Ho, Eds. *Laser Spectroscopy and Photochemistry on Metal Surfaces* (World Scientific, Singapore, 1995), pp. 625–1045; R. R. Cavanagh, D. S. King, J. C. Stephenson, T. F. Heinz, *J. Phys. Chem.* **97**, 786 (1993).
3. F.-J. Kao, D. G. Busch, D. Gomes da Costa, W. Ho, *Phys. Rev. Lett*. **70**, 4098 (1993); D. G. Busch and W. Ho, *ibid.* **77**, 1338 (1996).
4. S. Deliwala *et al.*, *Chem. Phys. Lett*. **242**, 627 (1995); R. J. Finlay, T. H. Her, C. Wu, E. Mazur, *ibid*. **274**, 499 (1997); T. H. Her, R. J. Finlay, C. Wu, E. Mazur, *J. Chem. Phys*. **108**, 8595 (1998).
5. A. Böttcher, H. Niehus, S. Schwegman, H. Over, G. Ertl, *J. Phys. Chem.* **B** 101, 11185 (1997).
6. K. L. Kostov, H. Rauscher, D. Menzel, *Surf. Sci.* **278**, 62 (1992).
7. F. Budde *et al.*, *Phys. Rev. Lett.* **66**, 3024 (1991).
8. J. A. Misewich, T. F. Heinz, D. M. Newns, *ibid*. **68**, 3737 (1992).
9. T. E. Madey, J. T. Yates Jr., D. A. King, C. J. Uhlaner, *J. Chem. Phys*. **52**, 5215 (1970).
10. M. Yata and R. J. Madix, *Surf. Sci.* **328**, 171 (1995).
11. The unoccupied $2\pi^*$ orbital of CO, thought to be relevant for electronically driven desorption [J. A. Prybyla, H. W. K. Tom, G. D. Aumiller, *Phys. Rev. Lett.* **68**, 503 (1992)], lies too far from the Fermi level [~5 eV; C. Benndorf *et al.*, *Surf. Sci.* **191**, 455 (1987)] to be accessible for the hot electrons, so that the desorption is phonon-driven.
12. We performed the density-functional theory (DFT) calculations using the pseudopotential plane wave method [M. Bockstedte, A. Kley, J. Neugebauer, M. Scheffler, *Comput. Phys. Commun.* **107**, 187 (1997); available at www.fhi-berlin.mpg.de/th/fhimd/] with the generalized gradient approximation (GGA) for the exchange-correlation functional. We use ab initio, fully separable, norm-conserving DFT-GGA pseudopotentials [N. Troullier and J. L. Martins, *Phys. Rev. B* **43**, 1991 (1993)] and take relativistic effects into account by using spin-averaged potentials. Further details can be found in (*17*). The calculated electronic eigenstates i are occupied according to the Fermi function f at finite temperatures, $f_i = f(\varepsilon_i, T_{el}) = [1 + \exp(\varepsilon_i - \varepsilon_F / k_B T_{el})]^{-1}$, where ε_F is the Fermi energy. The spatial electron density $n(r)$ is then optimized to minimize the free energy $F[T_{el};n] = E[T_{el};n] - T_{el} S[T_{el};n]$. Here, S denotes the entropy associated with the occupancy of the Kohn-Sham orbitals. With Fermi broadening, S reads [J. Neugebauer and M. Scheffler, *Phys. Rev. B* **46**, 16067 (1992)]:

$$S = -k_B \sum_i [f_i \ln f_i + (1 - f_i)\ln(1 - f_i)]$$

With this approach it is possible to study systems at high electronic temperatures by using density-functional theory.
13. M. Brandbyge *et al.*, *Phys. Rev. B* **52**, 6042 (1995).
14. L. M. Struck *et al.*, *Phys. Rev. Lett*. **77**, 4576 (1996).
15. S. I. Anisimov, B. L. Kapeliovich, T. L. Perel'man, *Zh. Eksp. Teor. Fiz*. **66**, 776 (1974) [*Sov. Phys. JETP* **39**, 375 (1974)]; S. I. Anisimov and B. Rethfeld, *Proc. SPIE* **3093**, 192 (1997).
16. In principle, τ_{el} is dependent on electron temperature and therefore on time (*13*), but the fact that the response in the two-pulse correlation measurement is slow compared with the pulse duration, and the proximity of the O electronic level to the Fermi level, imply $\tau_{el}(t) = \tau_{el}(0) = \tau_{el}$.
17. C. Stampfl, S. Schwegmann, H. Over, M. Scheffler, G. Ertl, *Phys. Rev. Lett*. **77**, 3371 (1996).
18. F. M. Hoffmann and M. D. Weisel, *Surf. Sci.* **253**, 59 (1991).

19. We gratefully acknowledge H.J. Bakker for helpful discussions. This work was supported in part by the Deutsche Forschungsgemeinschaft through SFB 450. The home page of the Ultrafast Surface Dynamics Group, Department of Physical Chemistry, Fritz-Haber-Institut, is available at www.fhi-berlin.mpg.de/pc/femtos/. M.B. thanks the European Community (TMR program) for financial support.

4 May 1999; accepted 22 June 1999